Optimization of Parameters for Atom Probe Tomography Analysis of -Tricalcium Phosphates

Selase Torkornoo, Marc Bohner, Ingrid McCarroll, Baptiste Gault

Microscopy and Microanalysis, 2024, **30**, 1074–1082
https://doi.org/10.1093/mam/ozae077
Advance access publication 30 August 2024
Original Article

Microscopy AND Microanalysis

Optimization of Parameters for Atom Probe Tomography Analysis of β-Tricalcium Phosphates

Selase Torkornoo[1,*], Marc Bohner[2], Ingrid McCarroll[1], and Baptiste Gault[1,3]

[1]*Department of Microstructure Physics and Alloy Design, Max Planck Institute für Eisenforschung, Max Planck Straße 1, 40237 Düsseldorf, Germany*
[2]*Research & Knowledge Transfer, RMS Foundation, Bischmattstrasse 12, 2544 Bettlach, Switzerland*
[3]*Department of Materials, Imperial College London, Royal School of Mines, Exhibition Road, London SW7 2AZ, UK*

***Corresponding author:** Selase Torkornoo, E-mail: s.torkornoo@mpie.de

Abstract

The biocompatibility and resorption characteristics of β-tricalcium phosphate (β-TCP, $Ca_3(PO_4)_2$) have made it a coveted alternative for bone grafts. However, the underlying mechanisms governing the biological interactions between β-tricalcium phosphate and osteoclasts remain elusive. It has been speculated that the composition at grain boundaries might vary and affect β-TCP resorption properties. Atom probe tomography (APT) offers a quantitative approach to assess the composition of the grain boundaries, and thus advance our comprehension of the biological responses within the microstructure and chemical composition at the nanoscale. The precise quantitative analysis of chemical composition remains a notable challenge in APT, primarily due to the influence of measurement conditions on compositional accuracy. In this study, we investigated the impact of laser pulse energy on the composition of β-TCP using APT, aiming for the most precise Ca:P ratio and consistent results across multiple analyses performed with different sets of analysis conditions and on two different instruments.

Key words: atom probe tomography, β-tricalcium phosphate ($Ca_3(PO_4)_2$, β-TCP), chemical composition

Graphical Abstract

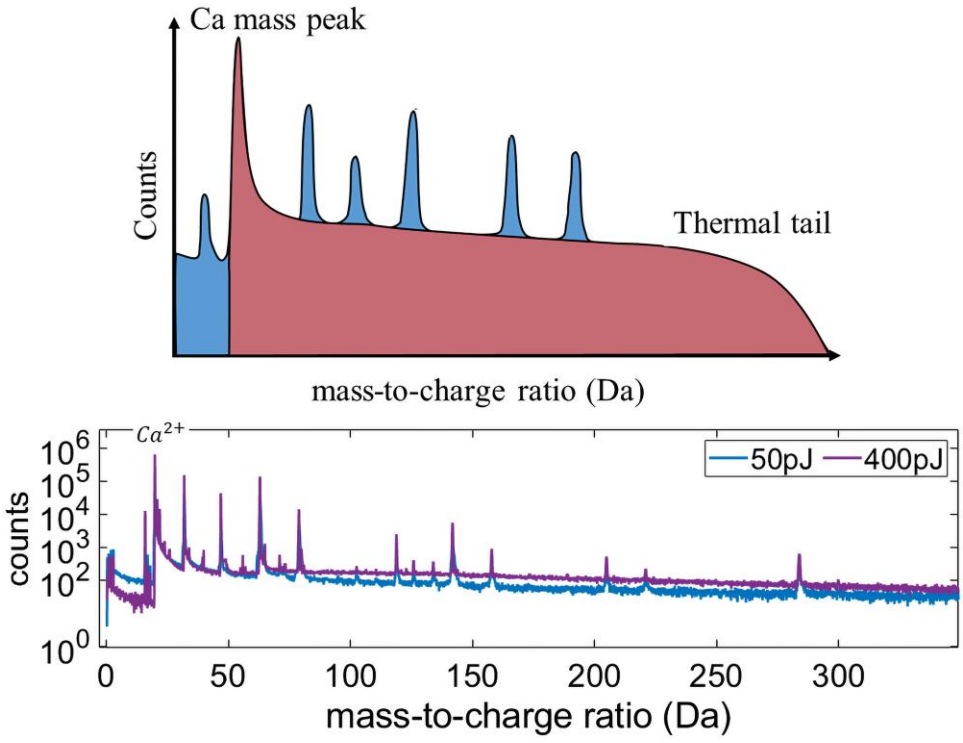

In laser-assisted APT, compositional analysis of β-tricalcium phosphate (β-TCP) is dependent on the balance between thermal tails, which is influenced by numerous experimental parameters, and the electrostatic field, which can be assessed through the use of a charge-state ratio. We provide the optimum APT analysis conditions for the most precise and chemical distributions of Ca and P in β-TCP.

Received: April 10, 2024. **Revised:** July 17, 2024. **Accepted:** August 6, 2024

Introduction

Bone loss is often associated to osteoarthritis, osteoporosis, and bone tumors resulting in locomotor disability, severe pain, morbidity, and loss of quality of life for the already aging global population (Zhang et al., 2022). Various alternatives exist to repair bone defects. Autologous bone grafts (e.g., self-derived), commonly called "autografts", require secondary surgical procedures and provoke complications, including donor site injury, morbidity, deformity, and scarring (Haugen et al., 2019). Hydroxyapatite (HA), β-tricalcium phosphate ($Ca_3(PO_4)_2$, β-TCP), HA-β-TCP biphasic mixtures, calcium-phosphate cements, and glass ceramics have been widely researched and applied as alternatives to autologous bone grafts because of their bone regenerative properties (Dimitriou et al., 2011). This study focused on β-TCP, a highly sought material for its excellent osteoclast-mediated resorptive and osteoinductive (Dimitriou et al., 2011; Le Gars Santoni et al., 2022, 2023; Humbert et al., 2024).

Even though β-TCP ability to resorb is well-established, contradictory statements are made regarding the rate of β-TCP resorption and the involved mechanism, i.e., chemical dissolution or osteoclast-mediated resorption. Small variations in the content of phase, chemical, and surface impurities have led to significant changes in *in vitro* osteoclastic resorption (Le Gars Santoni, 2022, 2023). Additionally, osteoclastic resorption leads to a needlelike structure suggesting bulk heterogeneities (Gallo et al., 2019; Bohner et al., 2020), in accordance with recent X-ray diffraction (XRD) results (Le Gars Santoni, 2020) and atomistic simulations (Sblendorio et al., 2023). Accordingly, it has been speculated that grain boundaries may play an important but still unexplored role (Bohner et al., 2020). Unfortunately, in-depth studies investigating the biological response beyond the macro- and micron-scale have been limited.

Atom probe tomography (APT) is an analytical technique in which individual atoms are removed in the form of ions from the surface of needle-shaped specimens by the application of an intense electrostatic field. This process is called field evaporation and is thermally activated. Time control over field evaporation is achieved by using high-voltage or laser pulses superimposed on a DC voltage. In laser pulsing mode, field evaporation is triggered by a thermal pulse arising from heat generated at the apex of the needle from absorption of the laser light (Miller, 1994). The respective ions' time-of-flight and impact position on a single-particle detector are used to reconstruct their 3D distribution, allowing compositional mapping on the nanoscale. By analyzing the distribution of species across a reconstructed dataset of β-TCP along with possible impurities, APT has the potential for advancing the understanding of the driving force behind the biological responses between β-TCP and osteoclasts, particularly in relation to the underlying microstructure of the consolidated material and its complex network of grain boundaries. The non-uniform dissolution of β-TCP microstructure by osteoclast using APT will be a topic of future research.

Here, we explored the influence of laser pulse energy (LPE) on the compositional analysis of β-TCP by APT to determine the most accurate and consistent compositions. APT is often thought to be a calibration-free quantitative technique; however, a strong sensitivity of the compositional measurement to the measurement conditions has been reported across almost all classes of materials amenable to APT analysis (Amouyal & Seidman, 2012; Mancini et al., 2014; La Fontaine et al., 2015). We discuss the descriptors used to compare data across multiple datasets. We finally report on the use of a new *in situ* coating approach, directly inside a focused-ion beam microscope (FIB), to prepare specimens for APT. The coating facilitates the rapid dissipation of heat from the apex of the needle and strengthens thin needles that would otherwise prematurely fracture due to thermal stress. The use of optimized APT parameters and an *in situ* FIB coating method provided a more accurate and precise understanding of the chemical heterogeneities potentially present in β-TCP.

Materials and Methods

Scanning Electron Microscopy and Focused-Ion Beam Sample Preparation

A layer of 20 nm carbon coating was sputtered onto cylinders of either 0.1 wt% Cu-doped β-TCP sintered in a standard atmosphere or pure β-TCP sintered in a monetite-rich atmosphere. Both were fabricated at the RMS Foundation, Switzerland, as described in Le Gars Santoni (2020). A 2.5 μm × 20 μm region of the β-TCP cylinder was coated with 0.5 μm of platinum carbon (Pt-C) using a gas-injection system inside a dual-beam scanning electron microscope/focused-ion beam (SEM/Ga FIB) (FEI Helios Nano-Lab 600i) (FEI Company, Hillsboro, OR, USA) at 3.0 kV and 1.4 nA. A trench was milled using a voltage of 30 kV and a current of 2.5 nA on each side of the Pt-C-coated lamella. Next, 3 μm × 3 μm of the lamella edge was milled at 30 kV and 0.79 nA to attach the 2.5 μm × 20 μm lamella to the OmniProbe 200 Nanomanipulator (Oxford Instruments, Abingdon, UK) with Pt-C. Lamella (2.5 μm × 2 μm) was mounted onto Presharpened Microtip™ Coupons (PSM M36) (CAMECA Instruments, Madison, WI, USA) and sharpened into needlelike shapes with a diameter of 30–100 nm. One of the sharpened specimens was coated with Cr using the *in situ* FIB coating method. For more details of the *in situ* FIB coating method, refer to Singh et al. (2023). The Cr sputtering was conducted at 30 kV and 40 pA for 20 s for each of the four sides by rotating the specimen 90°, 180°, and 90° after each pass.

Atom Probe Tomography

The Cu-doped specimens were analyzed using the laser pulsing mode in a local electrode atom probe, LEAP™ 5000 XS, and the nondoped specimens were analyzed in a LEAP 5000 XR. The LEAP™ 5000 XS has a straight flight path of 100 mm, a detection efficiency of approximately 80% and a 355 nm wavelength (ultraviolet) pulsed laser, focused onto a spot size below 5 μm with a 10 ps pulse duration. The data were collected using a range of LPEs from 50 to 400 pJ, a base temperature of 40 K, a repetition rate of 125 kHz and a fixed detection rate of 5 ions detected per 1,000 pulses on average. The Cu-doped β-TCP is analyzed in the atom probe with straight flight path because it has the potential to show the ion dissociation tracks unlike the atom probe fitted with a reflectron. This was to help better understand the mechanisms responsible for compositional biases.

The nondoped β-TCP is analyzed in the atom probe with a reflectron to explore possible analytical performance gains offered by using this instrument. The LEAP™ 5000 XR is fitted with a reflectron, has a flight path of 382 mm, a detection

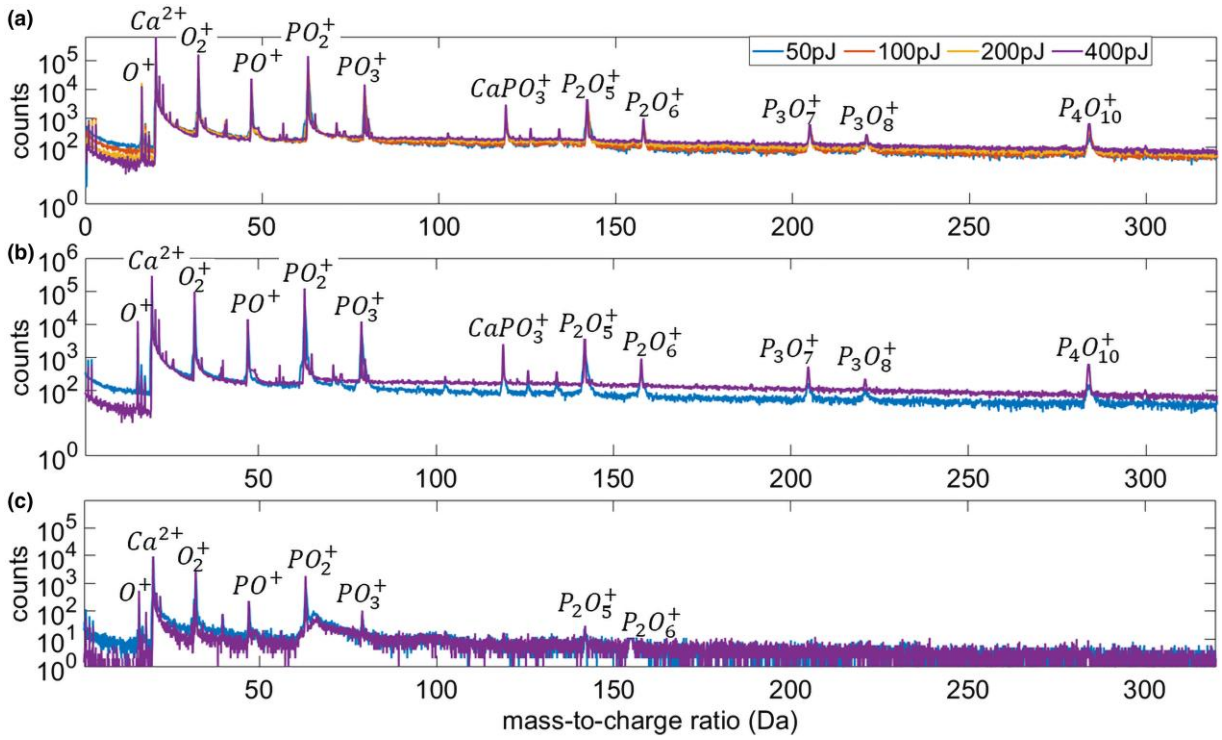

Fig. 1. The mass spectra of a β-TCP specimen at 50, 100, 200, and 400 pJ laser pulse energy along with a series of peaks at mass-to-charge ratios corresponding to atomic and molecular ions for (**a**) all events, (**b**) single event, and (**c**) double events.

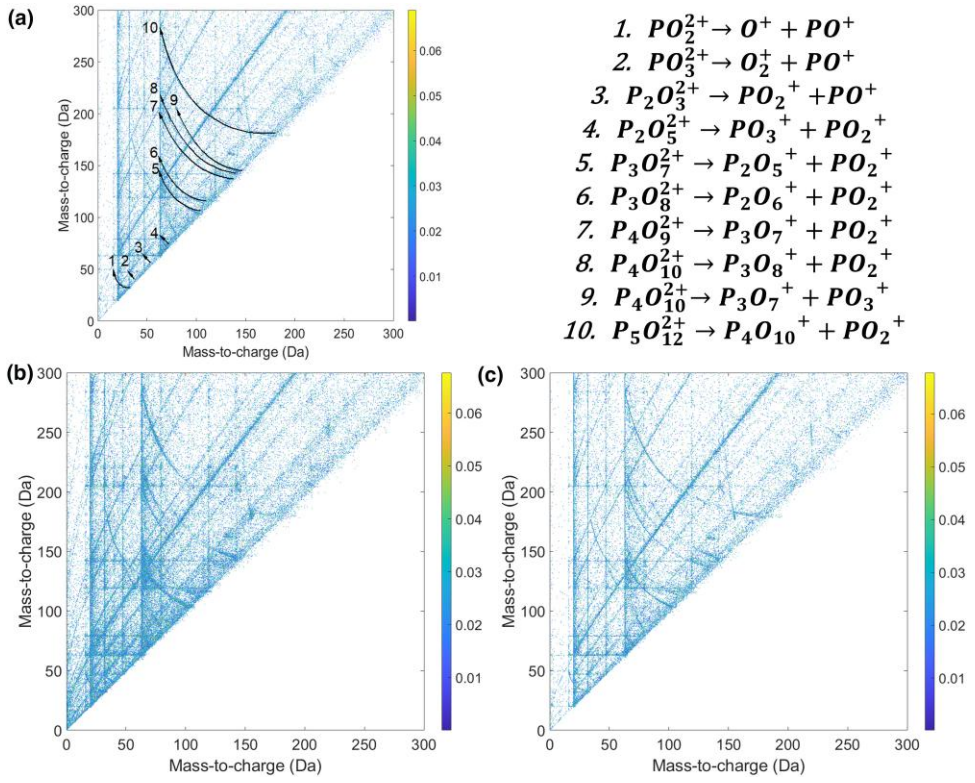

Fig. 2. The correlation histogram of multiples (**a**) with the dissociation tracks highlighted (**b**) using 50 pJ laser pulse energy (**c**) using 400 pJ laser pulse energy.

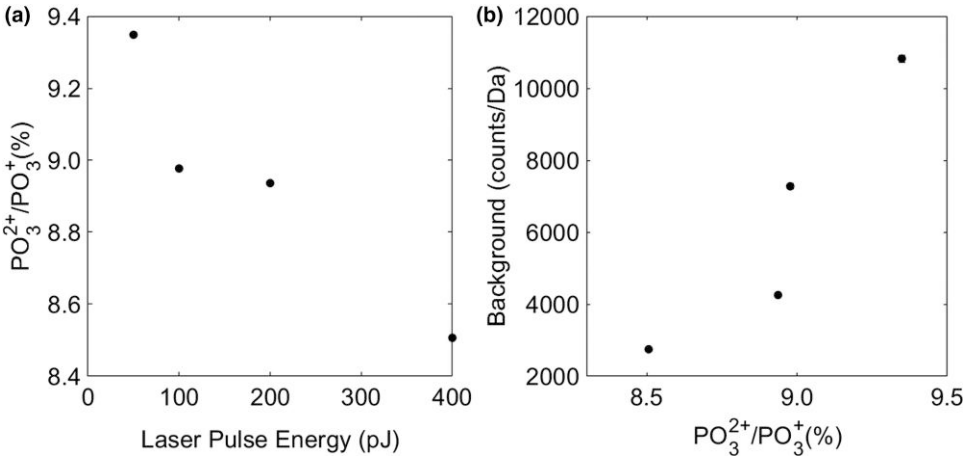

Fig. 3. The measurements of (**a**) PO_3^{2+}/PO_3^{+} charge-state ratio (%) plotted as a function of laser pulse energy (**b**) background noise plotted as a function of PO_3^{2+}/PO_3^{+} charge-state ratio (%).

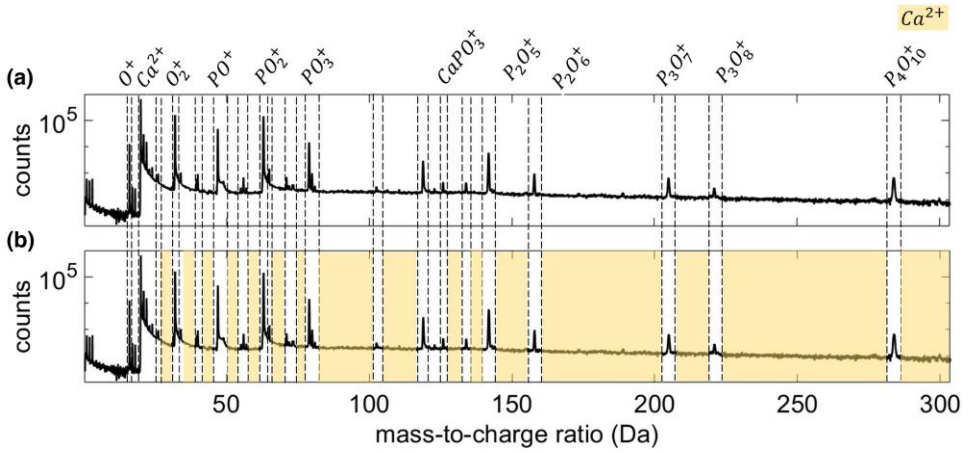

Fig. 4. The mass spectrum analysis of β-TCP along with a series of peaks at mass-to-charge ratios corresponding to (**a**) atomic and molecular ions, and (**b**) atomic and molecular ions including additional Ca^{2+} peaks from background presumed to be composed of mainly Ca ions.

efficiency of 52%, and a 355 nm wavelength (ultraviolet) pulsed laser, focused onto a spot size below 5 μm with a 10 ps pulse duration. The data were collected using a LPE of 150 pJ, a base temperature of 60 K, a repetition rate of 200 kHz, and the detection rate was fixed at 5 ions detected per 1,000 pulses on average. The processing and reconstruction of the datasets were performed in CAMECA Instruments APSUITE (version 6.3.0.90), and the data exported in APT format were further analyzed using MathWorks MATLAB (R2023b).

Table 1. Bulk Composition Determined in the Experiment of Figure 4.

	Atom Type						
	Ca	O	P	Na	H	Mg	Ca:P Ratio
A	23.7%	56.4%	19.5%	0.02%	0.38%	0.01%	1.21
B	26.5%	54.2%	18.8%	0.02%	0.36%	0.01%	1.41

Results

The mass spectra of the single β-TCP specimens obtained at 50, 100, 200, and 400 pJ LPEs show similar peak shapes, as shown in Figure 1a. The only marked difference is after the Ca^{2+} peak, where the background intensity increases substantially with increasing LPE. Multiple detection events for a single laser pulse are common for APT. Yao et al. (2010) suggested that plotting the mass spectra for single and multiple events separately can reduce the background and provide information on the field evaporation behavior of specific species. Here, the mass spectra for single and multiple events using 50 and 400 pJ LPEs are plotted in Figures 1b and 1c, respectively. The influence of the LPE is mostly visible for single events, with a relatively greater reduction in the background level with increasing LPE, which, in turn, leads to longer thermal tails of the mass peaks. The tails of the mass peaks are due to field evaporation occurring as the specimen cools down following heating by the laser pulse. This is particularly true for the thermal tail of the Ca^{2+} peak at 19.96 Da, which subsides quickly at lower LPEs but still extends over a very long range of mass-to-charge ratios.

The identification of unknown complex ions was facilitated by correlation histograms. The first dissociation track starts at the parent ion, PO_2^{2+}, corresponding to 31.5 Da, and ends at

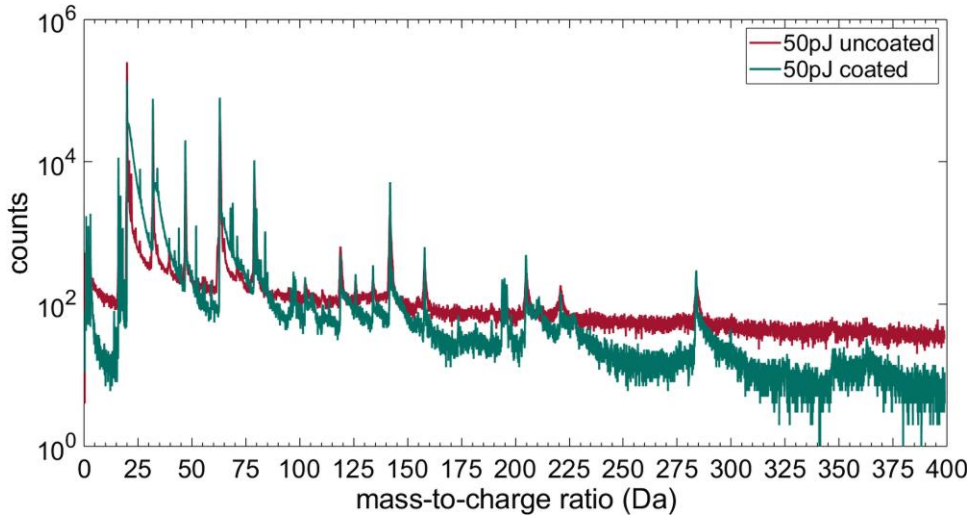

Fig. 5. The measurements of ions count plotted as a function of mass-to-charge ratio before and after coating along with a series of peaks at mass-to-charge ratios corresponding to atomic and molecular ions.

the daughter ions O^+ and PO^+, corresponding to 15.99 and 46.96 Da, respectively. The consecutive dissociation tracks are shown in Figure 2a. The intensity along the vertical line is highest and does not decrease for Ca^{2+} and PO_2^{2+} ions, corresponding to 19.96 and 62.95 Da, respectively. This indicates that Ca^{2+} and PO_2^{2+} ions are continuously generated, particularly in regions that correspond to the generation of other ionic species. Last, the overall intensity seen in Figure 2b is greater than that in Figure 2c. There are fewer hits at higher LPEs than at lower LPEs, indicating that some fragmentation is driven by the electrostatic field (Müller et al., 2011; Kirchhofer et al., 2013; Zanuttini et al., 2017).

To track the amplitude of the field across datasets and possibly instruments, we selected the PO_3^{2+}/PO_3^{+} charge-state ratio, which gradually decreased with increasing LPE, as shown in Figure 3a. This is consistent with the expected trend from post-ionization theory (Kingham, 1982). Accordingly, there is an increase in the background with increasing electrostatic field, as shown in Figure 3b. The background level measurements are acquired by ion counts per Da between 6 and 10 Da, a region in the mass spectrum presumed to be free of peaks. The standard errors of the charge-state ratio and background measurements were estimated based on the standard deviations of the statistical fluctuations, but they are smaller than the sizes of the symbols used in the graph. This can be explained by the large datasets sampled for this study. The background is related to the field evaporation of ions at DC voltage between laser pulses (Mancini et al., 2014). Laser pulses are used to trigger the time-of-flight measurement, which is used to determine the mass-to-charge ratio. Because field evaporation is not correlated with a pulse, the number of times of flight is not directly related to the mass-to-charge ratio of the ion, which hinders identification. At higher LPEs, the amplitude of the thermal pulse and the electrostatic field required to reach the set flux of ions are relatively lower, resulting in low rates of field evaporation between pulses. On the other hand, when using a lower LPE, a relatively high standing electrostatic field is sufficient to produce continuous field evaporation between pulses.

The Ca:P molar ratio according to the mass spectrum in Figure 4a is approximately 1.21, which is lower than the

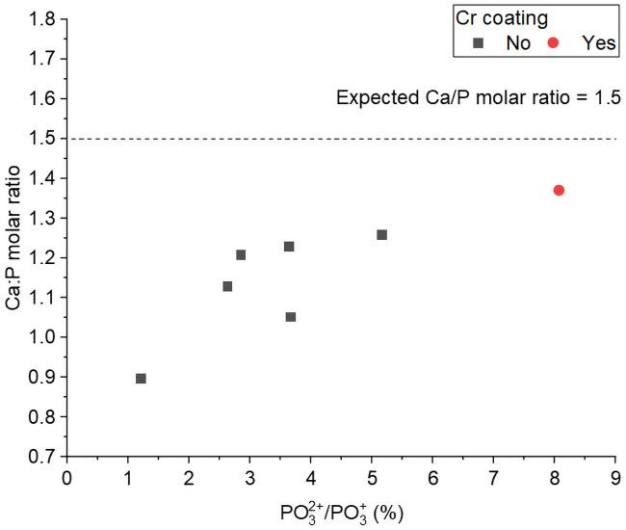

Fig. 6. The correlation of Ca:P molar ratio plotted as a function of PO_3^{2+}/PO_3^{+} charge-state ratio (%).

expected 1.5 Ca:P molar ratio acquired by XRD (Le Gars Santoni, 2020). Based on the correlation histograms, Ca^{2+} ions are continuously evaporated by the standing electrostatic field between pulses. All ions, including Ca^{2+} ions, detected between pulses are considered to be background noise. The Ca:P molar ratio increases to approximately 1.41 with the inclusion of additional Ca^{2+} peaks from the background, which we presume to be composed of mainly Ca^{2+} ions, as illustrated in Figure 4b. Table 1 summarizes the comparison of Ca:P molar ratios resulting in the inclusion of the Ca ions previously lost in the background of the mass spectrum. This analysis validates our hypothesis that the decrease in the Ca:P molar ratio is due to the exclusion of Ca ions from the background.

The application of a Cr coating on the specimen using the *in situ* FIB method introduced in Schwarz et al. (2024) reduces the background noise and specimen heating, as shown in Figure 5. The mass peak shape is indeed different, and the thermal tails of the major peaks (between 20 and 50 Da) of the coated specimen are indeed greater—i.e., the base of the peaks

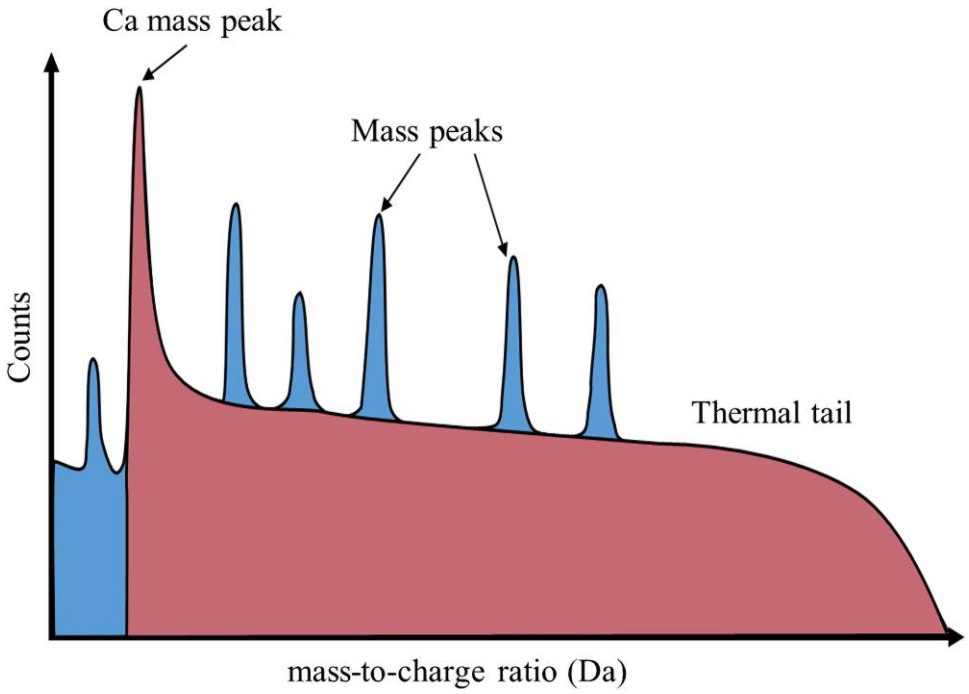

Fig. 7. Illustration of the effect of specimen tip heating on mass spectrum.

is wider—but with a steeper downward slope that indicates a faster return to the base temperature compared to the uncoated specimen. The mass spectrum of the coated specimen shows a significant reduction in the Ca^{2+} mass peak thermal tails caused by heating. This can be explained by the faster heat dissipation through the coated material. In Figure 6, the Ca:P molar ratio is plotted as a function of the PO_3^{2+}/PO_3^{+} ratio from data analyses performed on different specimens of the same material, with and without Cr coating, and the standard error is smaller than the size of the symbols used. The Ca:P molar ratio is the quotient of Ca and P. The Ca atom counts do not include the additional Ca^{2+} peaks from the background, which we presume to be composed of mainly Ca^{2+} ions. The PO_3^{2+}/PO_3^{+} charge-state ratios, which are indicative of the effect of the electrostatic field, were obtained using a $40 \times 40 \times 40$ nm cylinder containing an equal volume of atoms. There is a correlation between the electrostatic field and the Ca:P molar ratio. All the measured Ca:P molar ratios fall below the expected ratio of 1.5 but improve with increasing electrostatic field, particularly when a Cr coating is used.

Discussion

The study of β-TCP by APT appears challenging and requires a robust approach to achieve accurate results. Here, we aimed to find optimum experimental parameters for quantitative analysis, assessed based on the Ca:P molar ratio. There is an added level of complexity in evaluating the characteristics of insulating ceramic materials such as β-TCP by laser-assisted APT. The analytical performance of APT is dependent on the balance between the electrostatic field, which can be assessed through the use of a charge-state ratio, and the characteristics of the thermal pulse, which is known to be influenced by numerous experimental parameters (Bunton et al., 2007; Kelly et al., 2014). These properties are not easily tunable by APT operator-controlled parameters such as the LPE, laser pulse frequency, and specimen geometry.

In laser pulsing experiments where the LPE is systemically varied, a higher LPE generates a substantially higher background level after the Ca^{2+} peak compared to a lower LPE at first glance. This rise in background level is mainly from Ca^{2+} peak broadening at 19.96 Da, which is an outcome of the enlargement of the thermal tail shown in Figure 7. The mass spectra are similar to those previously reported in biomineral studies (Gordon et al., 2012; Pérez-Huerta et al., 2019; Schwarz et al., 2024). Peak broadening is caused by local thermal heating at the tip as the LPE increases (La Fontaine et al., 2016). The long thermal tails in the mass spectrum are due to the high specimen temperature necessary to facilitate field evaporation under the applied fields at higher LPEs and the low thermal diffusivity of oxides (Kirchhofer et al., 2013). The Ca^{2+} thermal tail subsides quickly at low LPEs, but still extends over a very long range of mass-to-charge state ratios according to the correlation histogram of multiples. Additionally, an increasing relative number of complex ions are undetectable at lower laser energies. Because the time-of-flight for heavy molecular ions is longer than the detection window, a slow pulsing rate is recommended to ensure that the majority of complex ions are detected as shown in Supplementary Figure S1. However, this has the undesirable side effect of increasing background noise.

Cr coating has the potential to improve Ca^{2+} mass peak resolution. The thermal tail at the Ca^{2+} mass peak, which originally extends over a very long range of mass-to-charge ratios, is reduced by approximately three times after the application of the Cr coating. The coated regions can quickly cool more than the uncoated regions. Although the new *in situ* FIB coating method reduces the Ca^{2+} thermal tail, revealing new peaks, the mass spectrum continues to show evidence of thermal tails caused by heating. The residual heating arises from the bottom half of the 5 μm long specimen tip, which is not adequately coated due to the specimen length as shown in Supplementary Figure S2. This

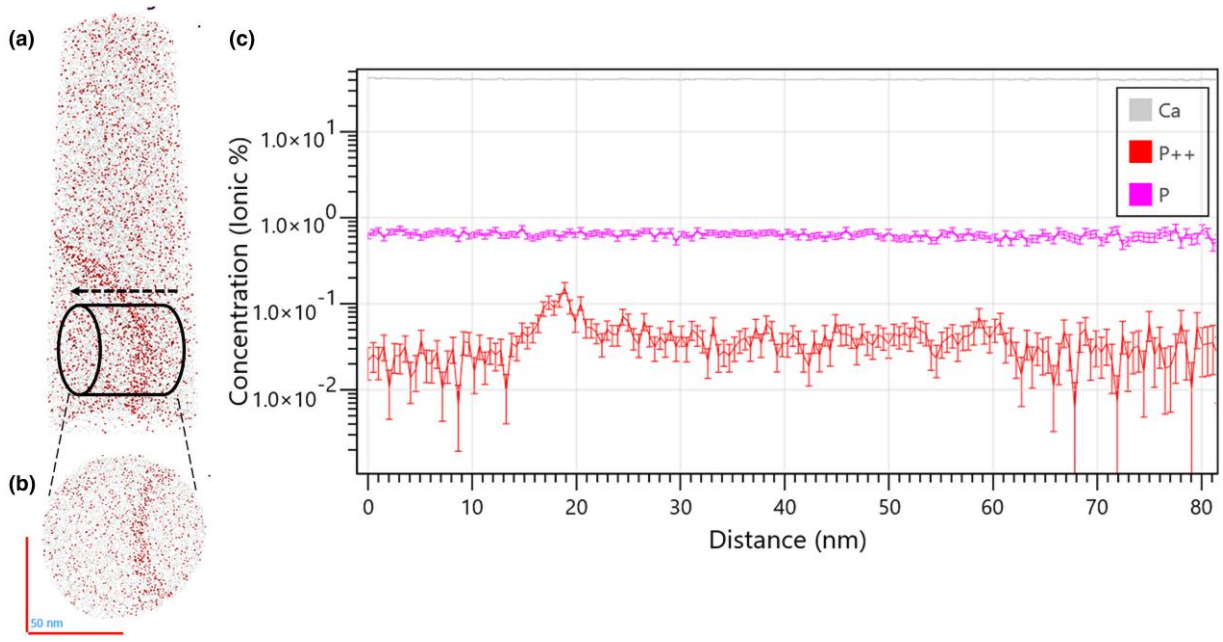

Fig. 8. Visualization of grain boundary interface; (**a**) side view of grain boundary surface, (**b**) top view of grain boundary surface, and (**c**) mass spectrum of the grain boundary interface with a higher fraction of P^{2+} ions.

highlights the importance of ensuring a conformal coating and optimizing specimen geometry for heat evacuation. The duration of the thermal pulse and the slope of the decay are primarily related to the specimen geometry (Bunton et al., 2007; Kelly et al., 2014). FIB preparation provides a way to control the specimen's end radius, shank angle and length.

By analyzing the ion counts utilizing high LPE, we determined a Ca:P molar ratio of approximately 1.21. The source of Ca depletion can be traced back to the thermal tail starting at 19.96 Da. Ca ions are ionized simultaneously as multiple complex ions containing phosphorus and between peaks according to the correlation histogram. Two or more ions that hit the detector simultaneously cannot be identified as two unique events and will result in a loss of detection of one of the ions (Peng et al., 2018). Ca ions are then not properly identified by the detector when multiple ions arrive at the same time. The molar ratio is then depreciated because the Ca ions detected simultaneously with other ions and between pulses are not included in the bulk composition analysis.

Further analysis of the mass spectrum revealed the electrostatic field as a variable impacting the accuracy of the bulk compositional analysis. The Ca:P molar ratios measured at relatively higher electrostatic fields appear to be more accurate than those measured at lower electrostatic fields. The molar fractions of P, Ca, and O are also a function of field, not LPE (see Supplementary Fig. S3). The stoichiometry of the oxide deviates from known values due to varying evaporation rates of Ca, P, and O ions during measurements. The energy required to remove atoms from a surface is different for each ion type, which can be explained by Müller's evaporation-field formula. Müller defines the energy, Q_o, required to ionize an atom before an electric field is applied to the tip as

$$Q_o = \Lambda + \sum_i^n I_i - \Phi_e, \tag{1}$$

where Λ is the sublimation energy, I_i is the ith ionization energy, and Φ_e is the work function of the surface emitting the ion. In the presence of an applied electric field, the energy barrier, Q(F), is written as

$$\mathrm{Q(F)} = Q_o - \sqrt{\frac{n^3 e^3}{4\pi\varepsilon_o} F}, \tag{2}$$

where ε_o is the dielectric permittivity of the vacuum and F is the electric field. For field evaporation, F_{evap}, the field at which the energy barrier is zero, is expressed as

$$F_{\mathrm{evap}} = \frac{4\pi\varepsilon_o}{n^3 e^3}(Q_o)^2. \tag{3}$$

When the applied electric field is near the field evaporation, Eq. (2) can be rewritten as

$$\mathrm{Q(F)} = Q_o - Q_o\sqrt{\frac{F}{F_{\mathrm{evap}}}} \approx Q_o\left(1 - \frac{F}{F_{\mathrm{evap}}}\right). \tag{4}$$

The rate of field evaporation is expressed as

$$\Phi_{\mathrm{evap}} = \nu_0 \exp\left(-\frac{Q(F)}{k_B T}\right), \tag{5}$$

where ν_0 is the atomic vibrational frequency of the field-adsorbed atom, k_B is the Boltzmann constant, and T is the absolute temperature. The relationship between the electric field and field of evaporation can be shown as a function of temperature,

$$\frac{F}{F_{\mathrm{evap}}} \approx 1 + 2\ln\left(\frac{\Phi_{\mathrm{evap}}}{\nu_0}\right)^2 \frac{k_B T}{Q_o}. \tag{6}$$

This further explains the result of specimen heating in the field of evaporation observed experimentally in this study, e.g., by Marquis & Gault (2008).

The ionization energy also varies greatly for the various elemental species, and further analysis is needed to understand the tradeoffs. Per Tsong, a simplified expression for the field of

evaporation for an ion is proportional to $e^{\left(-\frac{I^3}{eF}\right)}$. Ca has first and second ionization energies of 6 and 12 eV, respectively, while the first and second ionization energies of P are 10 and 20 eV, respectively (Tsong, 1978). Using first ionization energies as a proxy for the evaporation field, the field of evaporation for Ca is greater than that for P. Consequently, the evaporation rate of Ca is suppressed at low electrostatic fields with respect to P. Several studies have shown that the stoichiometry of the oxide deviates from known values when the background noise level is low at high LPEs (Kirchhofer et al., 2013) and that the expected ratio is consistent when using moderate laser energy (10–100 pJ) (Valderrama et al., 2015). This is also consistent with the observations in this study.

With the completion of this groundwork, our goal was to perform further analyses of β-TCP, particularly at grain boundaries. These can be difficult to target during specimen preparation due to charging and a lack of contrast during the last stages of FIB-based specimen preparation. Figure 8 displays APT data from a pure β-TCP prepared in a monetite-rich atmosphere. Within this longer dataset, we can observe a change in the distribution of the charge states locally, particularly the appearance of a peak of P^{2+} that is segregated along a planar feature. This localized change in the field can be attributed to the presence of a grain boundary (Oberdorfer et al., 2013; Wei et al., 2019). A composition profile through this interface reveals the same composition on either side and no specific segregation of any other elements. The Ca:P ratio appears to be maintained across this specific grain boundary.

Conclusion

To further understand the osteoclastic resorption properties of β-TCP, the chemical distribution of calcium and impurities in β-TCP need to be closely examined. Although preliminary efforts to obtain accurate chemical distributions of Ca and P in β-TCP have thus far proven to be unattainable using APT, further optimization of APT parameters will provide a more precise understanding of the chemical distribution within β-TCP, in particular at grain boundaries.

- The measured molar ratio is consistent with known values obtained using low laser energy (i.e., 10–100 pJ).
- A lower pulsing rate (i.e., 125 kHz) increases the likelihood of detecting complex ions containing phosphorus, thereby improving the accuracy of the molar ratio.
- The source of Ca depletion can be traced back to the thermal tail starting at 20 Da.
- The *in situ* FIB coating method highlights the importance of coatings or other means for specimen heat removal.

Availability of Data and Materials

The authors have declared that no datasets apply for this piece.

Supplementary Material

To view supplementary material for this article, please visit https://doi.org/10.1093/mam/ozae077.

Acknowledgments

The authors are grateful to Bastien Le Gars Santoni for the synthesis of the β-TCP samples. The authors acknowledge the support for this work from Uwe Tezins, Andreas Sturm, and Christian Broß for their support to the APT, SEM, FIB, and metallography facilities at Max-Planck-Institut für Eisenforschung GmbH. The authors are grateful to Dr. Markus Kühbach for sharing the code to open.APT files (see also https://github.com/mkuehbach/PARAPROBE). The authors also grateful to Eric Woods, Tim Schwarz, Raymond Kwesi Nutor, and Shyam Katnagallu for their insightful feedback, discussions, and support.

Financial Support

I.M. and B.G. are grateful for funding from the European Research Council (ERC) for the project SHINE (ERC-CoG) #771602. B.G., I.M., and S.T. are grateful to the Deutsche Forschungsgemeinschaft (DFG) for funding through B.G.'s Leibniz Award.

Conflict of Interest

The authors declare that they have no competing interest.

References

Amouyal Y & Seidman DN (2012). Atom-probe tomography of nickel-based superalloys with green or ultraviolet lasers: A comparative study. *Microsc Microanal* **18**, 971–981. https://doi.org/10.1017/S1431927612001183

Bohner M, Le Gars Santoni B & Döbelin N (2020). β-tricalcium phosphate for bone substitution: Synthesis and properties. *Acta Biomater* **113**, 23–41. https://doi.org/10.1016/j.actbio.2020.06.022

Bunton JH, Olson JD, Lenz DR & Kelly TF (2007). Advances in pulsed-laser atom probe: Instrument and specimen design for optimum performance. *Microsc Microanal* **13**, 418–427. https://doi.org/10.1017/S1431927607070869

Dimitriou R, Jones E, McGonagle D & Giannoudis PV (2011). Bone regeneration: Current concepts and future directions. *BMC Med* **9**, 66. https://doi.org/10.1186/1741-7015-9-66

Gallo M, Le Gars Santoni B, Douillard T, Zhang F, Gremillard L, Dolder S, Hofstetter W, Meille S, Bohner M, Chevalier J & Tadier S (2019). Effect of grain orientation and magnesium doping on β-tricalcium phosphate resorption behavior. *Acta Biomater* **89**, 391–402. https://doi.org/10.1016/j.actbio.2019.02.045

Gordon LM, Tran L & Joester D (2012). Atom probe tomography of apatites and bone-type mineralized tissues. *ACS Nano* **6**, 10667–10675. https://doi.org/10.1021/nn3049957

Haugen HJ, Lyngstadaas SP, Rossi F & Perale G (2019). Bone grafts: Which is the ideal biomaterial? *J Clin Periodontol* **46**, 92–102. https://doi.org/10.1111/jcpe.13058

Humbert P, Kampleitner C, De Lima J, Brennan MÁ, Lodoso-Torrecilla I, Sadowska JM, Blanchard F, Canal C, Ginebra M-P, Hoffmann O & Layrolle P (2024). Phase composition of calcium phosphate materials affects bone formation by modulating osteoclastogenesis. *Acta Biomater* **176**, 417–431. https://doi.org/10.1016/j.actbio.2024.01.022

Kelly TF, Vella A, Bunton JH, Houard J, Silaeva EP, Bogdanowicz J & Vandervorst W (2014). Laser pulsing of field evaporation in atom probe tomography. *Curr Opin Solid State Mater Sci* **18**, 81–89. https://doi.org/10.1016/j.cossms.2013.11.001

Kingham DR (1982). The post-ionization of field evaporated ions: A theoretical explanation of multiple charge states. *Surf Sci* **116**, 273–301. https://doi.org/10.1016/0039-6028(82)90434-4

Kirchhofer R, Teague MC & Gorman BP (2013). Thermal effects on mass and spatial resolution during laser pulse atom probe tomography of cerium oxide. *J Nucl Mater* **436**, 23–28. https://doi.org/10.1016/j.jnucmat.2012.12.052

La Fontaine A, Gault B, Breen A, Stephenson L, Ceguerra AV, Yang L, Dinh Nguyen T, Zhang J, Young DJ & Cairney JM (2015). Interpreting atom probe data from chromium oxide scales. *Ultramicroscopy* **159**, 354–359. https://doi.org/10.1016/j.ultramic.2015.02.005

La Fontaine A, Zavgorodniy A, Liu H, Zheng R, Swain M & Cairney J (2016). Atomic-scale compositional mapping reveals Mg-rich amorphous calcium phosphate in human dental enamel. *Sci Adv* **2**, e1601145. https://doi.org/10.1126/sciadv.1601145

Le Gars Santoni B (2020). *Ion-Doped Grain Boundaries to Control the Dissolution as Well as the Osteoclastic and Macrophage Response of Sintered Calcium Phosphate Ceramics*. Bern: University of Bern.

Le Gars Santoni B, Niggli L, Dolder S, Loeffel O, Sblendorio GA, Heuberger R, Maazouz Y, Stähli C, Döbelin N, Bowen P, Hofstetter W & Bohner M (2022). Effect of minor amounts of β-calcium pyrophosphate and hydroxyapatite on the physico-chemical properties and osteoclastic resorption of β-tricalcium phosphate cylinders. *Bioact Mater* **10**, 222–235. https://doi.org/10.1016/j.bioactmat.2021.09.003

Le Gars Santoni B, Niggli L, Dolder S, Loeffel O, Sblendorio GA, Maazouz Y, Alexander DTL, Heuberger R, Stähli C, Döbelin N, Bowen P, Hofstetter W & Bohner M (2023). Influence of the sintering atmosphere on the physico-chemical properties and the osteoclastic resorption of β-tricalcium phosphate cylinders. *Acta Biomater* **169**, 566–578. https://doi.org/10.1016/j.actbio.2023.08.012

Mancini L, Amirifar N, Shinde D, Blum I, Gilbert M, Vella A, Vurpillot F, Lefebvre W, Lardé R, Talbot E, Pareige P, Portier X, Ziani A, Davesnne C, Durand C, Eymery J, Butté R, Carlin J-F, Grandjean N & Rigutti L (2014). Composition of wide bandgap semiconductor materials and nanostructures measured by atom probe tomography and its dependence on the surface electric field. *J Phys Chem C* **118**, 24136–24151. https://doi.org/10.1021/jp5071264

Marquis EA & Gault B (2008). Determination of the tip temperature in laser assisted atom-probe tomography using charge state distributions. *J Appl Phys* **104**, 084914. https://doi.org/10.1063/1.3006017

Miller MK (1994). Atom probe field ion microscopy. *Vacuum* **45**(6–7), 819–831. https://doi.org/10.1016/0042-207X9490117-1

Müller M, Saxey DW, Smith GDW & Gault B (2011). Some aspects of the field evaporation behaviour of GaSb. *Ultramicroscopy* **111**(6), 487–492. https://doi.org/10.1016/j.ultramic.2010.11.019

Oberdorfer C, Eich SM & Schmitz G (2013). A full-scale simulation approach for atom probe tomography. *Ultramicroscopy* **128**, 55–67. https://doi.org/10.1016/j.ultramic.2013.01.005

Peng Z, Vurpillot F, Choi P-P, Li Y, Raabe D & Gault B (2018). On the detection of multiple events in atom probe tomography. *Ultramicroscopy* **189**, 54–60. https://doi.org/10.1016/j.ultramic.2018.03.018

Pérez-Huerta A, Suzuki M, Cappelli C, Laiginhas F & Kintsu H (2019). Atom probe tomography (APT) characterization of organics occluded in single calcite crystals: Implications for biomineralization studies. *C—J Carbon Res* **5**, 50. https://doi.org/10.3390/c5030050

Sblendorio GA, Le Gars Santoni B, Alexander DTL, Bowen P, Bohner M & Döbelin N (2023). Towards an improved understanding of the β-TCP crystal structure by means of "checkerboard" atomistic simulations. *J Eur Ceram Soc* **43**(8), 3746–3754. https://doi.org/10.1016/j.jeurceramsoc.2023.02.036

Schwarz TM, Woods E, Singh MP, Chen X, Jung C, Aota LS, Jang K, Krämer M, Kim S-H & McCarroll I (2024). In situ metallic coating of atom probe specimen for enhanced yield, performance, and increased field-of-view. *Microsc Microanal*, 1–15. https://doi.org/10.1093/mam/ozae006

Singh MP, Woods EV, Kim S-H, Jung C, Aota LS & Gault B (2023). Facilitating the systematic nanoscale study of battery materials by atom probe tomography through in-situ metal coating. *Batter Supercaps* **7**(2). https://doi.org/10.1002/batt.202300403

Tsong TT (1978). Field ion image formation. *Surf Sci* **70**(1), 211–233. https://doi.org/10.1016/0039-60287890410-7

Valderrama B, Henderson HB, Gan J & Manuel MV (2015). Influence of instrument conditions on the evaporation behavior of uranium dioxide with UV laser-assisted atom probe tomography. *J Nucl Mater* **459**, 37–43. https://doi.org/10.1016/j.jnucmat.2014.12.119

Wei Y, Peng Z, Kühbach M, Breen A, Legros M, Larranaga M, Mompiou F & Gault B (2019). 3D nanostructural characterisation of grain boundaries in atom probe data utilising machine learning methods. *PLoS One* **14**(11), e0225041. https://doi.org/10.1371/journal.pone.0225041.

Yao L, Gault B, Cairney JM & Ringer SP (2010). On the multiplicity of field evaporation events in atom probe: A new dimension to the analysis of mass spectra. *Philos Mag Lett* **90**(2), 121–129. https://doi.org/10.1080/09500830903472997

Zanuttini D, Blum I, Rigutti L, Vurpillot F, Douady J, Jacquet E, Anglade P-M & Gervais B (2017). Simulation of field-induced molecular dissociation in atom-probe tomography: Identification of a neutral emission channel. *Phys Rev A* **95**(6), 061401. https://doi.org/10.1103/PhysRevA.95.061401

Zhang Z, Zhou J, Liu C, Zhang J, Shibata Y, Kong N, Corbo C, Harris MB & Tao W (2022). Emerging biomimetic nanotechnology in orthopedic diseases: Progress, challenges, and opportunities. *Trends Chem* **4**(5), 420–436. https://doi.org/10.1016/j.trechm.2022.02.002